Mussel-inspired agarose hydrogel scaffolds for skin tissue engineering

Ting Su[a,b,c,d], Mengying Zhang[b], Qiankun Zeng[b], Wenhao Pan[a,b], Yijing Huang[d], Yuna Qian[b], Wei Dong[d], Xiaoliang Qi[a,b,*], Jianliang Shen[a,b,**]

[a] State Key Laboratory of Ophthalmology, Optometry and Vision Science, School of Ophthalmology and Optometry, School of Biomedical Engineering, Wenzhou Medical University, Wenzhou, 325027, China
[b] Engineering Research Center of Clinical Functional Materials and Diagnosis & Treatment Devices of Zhejiang Province, Wenzhou Institute, University of Chinese Academy of Sciences, Wenzhou, 325001, China
[c] School of Chemistry & Materials Engineering, Fuyang Normal University, Fuyang, 236037, China
[d] School of Chemical Engineering, Nanjing University of Science & Technology, Nanjing, 210094, China

ABSTRACT

Polysaccharide hydrogels are widely used in tissue engineering because of their superior biocompatibility and low immunogenicity. However, many of these hydrogels are unrealistic for practical applications as the cost of raw materials is high, and the fabrication steps are tedious. This study focuses on the facile fabrication and optimization of agarose-polydopamine hydrogel (APG) scaffolds for skin wound healing. The first study objective was to evaluate the effects of polydopamine (PDA) on the mechanical properties, water holding capacity and cell adhesiveness of APG. We observed that APG showed decreased rigidity and increased water content with the addition of PDA. Most importantly, decreased rigidity translated into significant increase in cell adhesiveness. Next, the slow biodegradability and high biocompatibility of APG with the highest PDA content (APG3) was confirmed. In addition, APG3 promoted full-thickness skin defect healing by accelerating collagen deposition and promoting angiogenesis. Altogether, we have developed a straightforward and efficient strategy to construct functional APG scaffold for skin tissue engineering, which has translation potentials in clinical practice.

1. Introduction

Hydrogels with a high percentage of water in their three-dimensional network have been shown to mimic the extracellular matrix (ECM) better [1–3]. They play an essential role in the development of tissue engineering scaffolds because of their ability to provide microenvironments for cell adhesion, proliferation and migration, and to promote the exchange of biomolecules, while not affecting their biological activity [4,5]. The mechanical parameters of hydrogel scaffolds will be sensed by cells and affect the cell behavior [6–8]. An idea hydrogel scaffold requires to match the tissue and ECM mechanics [9,10,11]. As living tissues and ECMs exhibit complex, time/rate dependent mechanical behaviors, it is essential to construct a hydrogel platform with adjustable mechanical strength.

Over the past decade, the use of hydrogel in wound dressing has been widely studied. Hydrogel dressings can create a moist wound environment that is beneficial for skin tissue regeneration [12,13]. Most of the reported hydrogel dressings are based on synthetic polymers and natural polymers (such as polysaccharide and protein) [14–17]. Unfortunately, these polymers have certain drawbacks when used alone. For example, synthetic polymer hydrogel lacks biological activity and has a certain degree of cytotoxicity, polysaccharide hydrogels are usually difficult to control the mechanical properties and often needs additional crosslinking agents to improve the weak mechanical strength, and protein hydrogels are costly and unstable under human body conditions.

An ideal wound dressing should be easy to prepare, biocompatible, cell adhesive and having appropriate mechanical properties. This study focuses on the design and optimization of agarose-polydopamine composite scaffolds for skin tissue engineering. Agarose is a fascinating polysaccharide due to its controlled self-gelling properties [18–20]. The formed agarose hydrogels have adjustable mechanical properties and
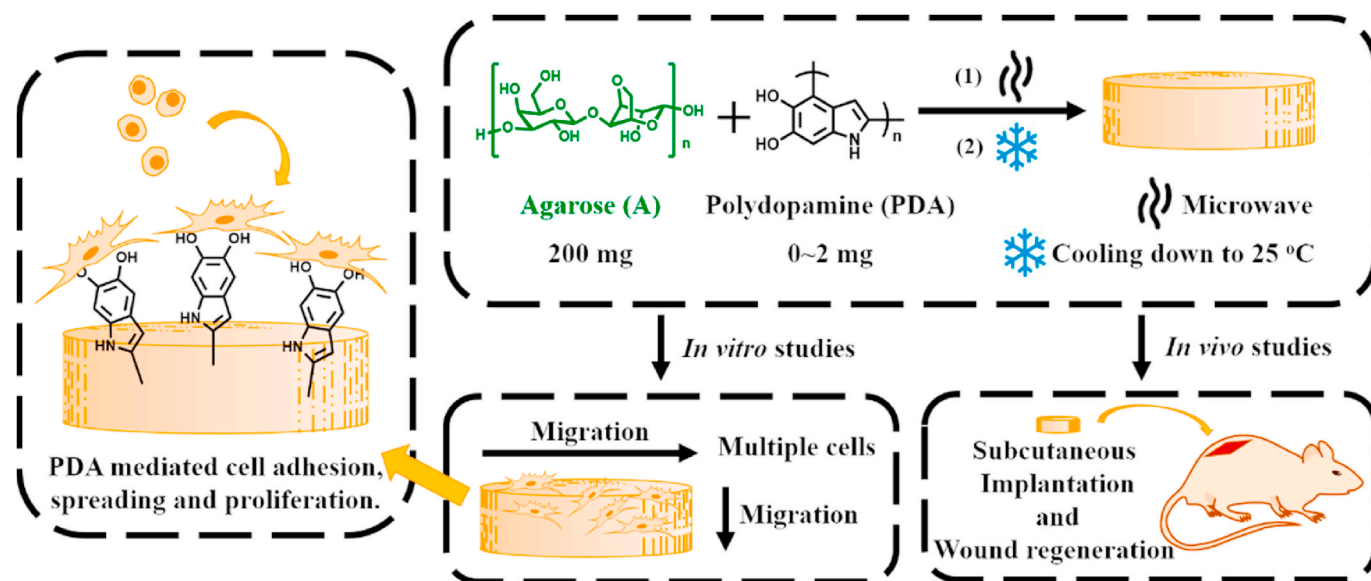
Fig. 1. Schematic illustration of agarose-PDA hydrogels for cell culture and tissue engineering.

Table 1
Feeding ratio of agarose-PDA hydrogels with different compositions.

Composition	Designation			
	AHG	APG1	APG2	APG3
Agarose (g)	0.2	0.2	0.2	0.2
PDA solution (mL)	0.0	2.5	5.0	10.0
DW (mL)	10.0	7.5	5.0	0.0

tunable water adsorption capacity, which hold great potentials for various tissue engineering applications. PDA, originating from the foot protein of mussels, is a powerful tool for the development of new functional hydrogels [21–23]. It has abundant functional groups (such as imine, amine and catechol groups) that can interact with various surfaces/molecules through hydrogen bonds, electrostatic interactions and π-π stacking [24–27]. Previous studies have confirmed that the incorporation of PDA can endow polysaccharide hydrogel material with appealing functions, such as controlled drug delivery, photo-thermal therapy and tissue/cell adhesive properties [24,28–30].

With these considerations in mind, herein we developed APG scaffolds for skin tissue engineering. The APG was synthesized through simple step (Fig. 1). The mechanical properties of APG were easily controlled by adjusting the content of PDA in APG. Both *in vitro* and *in vivo* investigations demonstrated the biocompatibility and biodegradability of APG3. The cell migration rate of MRC-5 and RS1 cells on the surface of APG3 is high and the cells can migrate from the surface to the inside of APG3. Moreover, such APG3 could facilitate wound healing by accelerating collagen deposition and promoting vascularization. These findings demonstrate its potential in skin tissue engineering, and also provide support for its application in drug delivery and regenerative medicine.

2. Materials and methods

2.1. Materials

Agarose and sodium hydroxide (NaOH) were purchased from Aladdin (Shanghai, China). 3-Hydroxytyramine hydrochloride (dopamine hydrochloride, DAHC) was purchased from Energy Chemical (Shanghai, China). Cell Counting Kit (CCK)-8 and LIVE/DEAD Viability Kit were purchased from Beyotime Biotechnology (Shanghai, China).

FITC Phalloidin and DiIC18(3) were purchased from Solarbio (Beijing, China). Rabbit antiβ1-integrin and goat anti-rabbit integrin were purchased from Abcam (Shanghai, China). Deionized water (DW) and phosphate-buffered saline (PBS) were used throughout this study. All reagents were used as received.

2.2. Fabrication of pure agarose hydrogel (AHG) and APG

The AHG and APG were fabricated by a simple process (Fig. 1). Briefly, the PDA solution was made by dissolving DAHC (0.2 mg/mL) in NaOH (aq, pH = 8), and the oxidation reaction was carried out under ambient conditions (25 °C, 24 h, with magnetic stirring). Then, the PDA solution was serially diluted in DW to obtain PDA solutions with different concentrations (Table 1). Next, 0.2 g of agarose was added to each solution, and microwave heating was used to dissolve the added agarose. The resulting hot, thick, homogeneous solution transformed into a gel (within 10 min) when spontaneously cooled.

To determine the PDA concentration in APG3, a series of PDA calibration solution standards was prepared and measured to plot the calibration curve (Figure S1A–S1B). Then, 10 g of freshly prepared APG3 was soaked in 50 mL DW to remove the unchained PDA. This 50 mL DW solution was changed once a day for 4 days, and the soaking solutions were collected and mixed. The concentration of PDA (0.0046 mg/mL) in the soaking solutions of APG3 was calculated using UV–vis spectroscopy (Figure S1C). The released weight of PDA after soaking was 0.92 mg, and this meant that we could assume that the content of PDA in APG3 was 1.08 mg.

2.3. Characterization of APG

FTIR spectra were recorded on a Bruker Tensor II spectrometer to confirm the structure and functional groups of the AHG and APG. The background was subtracted, and the scanning was performed in the range of 400–4000 cm^{-1}. X-ray diffraction (XRD) measurements were performed on a Bruker D8 diffraction meter to assess the crystalline structure of agarose, AHG, and APG. The patterns of Cu Kα radiation at 40 kV and 40 mA were recorded in the *2θ* range of 5–70°. Thermogravimetric analysis (TGA) was performed on PerkinElmer TGA8000 thermal gravimetric analyzer under nitrogen atmosphere (50–600 °C, 10 °C/min). The TA DHR-2 rheometer was used to assess rheology. A frequency sweep was conducted with parallel plate geometry (25 mm diameter) and a 1 mm gap distance in the frequency

range of 0.1–100 Hz. Fixed strain ($\gamma = 1\%$) was employed to ensure the linearity of viscoelasticity. To characterize the mechanical properties of the freshly prepared AHG and APG, a UPW2102 electronic universal testing machine was used. The hydrogels were made into a cylinder (3 cm in diameter and 5 cm in height), and compression tests were performed at a rate of 2 mm/min. The porous morphology of the xerogel was captured by field emission scanning electron microscopy (FESEM, HITACHI, SU8010). Before observation, all the samples were cut into cubes, freeze-dried, and sputter-coated with platinum. The pore sizes were calculated using the Nano Measurer 1.2.5 software (Fudan University).

2.4. Swelling and de-swelling behavior

2.4.1. Swelling test

The lyophilized hydrogels were placed in four types of immersion fluid (DW, NaCl solution, $MgCl_2$ solution, and $AlCl_3$ solution). The weight of the sample was recorded before soaking (W_0) and after soaking for time t (W_t). The swelling ratio (SR) was calculated as follows:

$$SR = W_t/W_0$$

2.4.2. De-swelling

Dry AHG and APG were soaked in DW at room temperature until they reached the weight balance. The weights of the fully swollen hydrogels were recorded (W_0). Then these hydrogels were transferred to a wind-drying oven where the de-swelling process occurred at 37 °C. At specified time points, the weights of the samples were measured (W_t), and water retention (WR) was defined as follows:

$$WR\,(\%) = (W_t/W_0) \times 100$$

2.5. Cell culture

Four types of cells (MRC-5, RS1, NIH3T3, and DPSC) were used for these experiments. The culture medium was DMEM (Gibco, for MRC-5, RS1, and NIH3T3) and α-DMEM (Gibco, for DPSC), containing 10% fetal bovine serum (FBS, Gibco) and 1% penicillin/streptomycin (PS, Gibco). The cells were incubated at 37 °C and 5% CO_2.

2.6. Cytotoxicity

The cytotoxicity of AHG and APG toward MRC-5 and RS1 was examined by the CCK-8 assay. First, AHG and APG were soaked in 75% alcohol, and after sterilization, the hydrogels were separately immersed in PBS and DMEM to remove the residual alcohol. Cells were seeded onto 24-well plates at a density of 2×10^4 (for MRC-5) and 5×10^3 (for RS1) cells per well with 1 mL of DMEM medium. After a 24 h incubation, sterilized hydrogels (3.4 mg/mL) were added into each well. Cells incubated without samples were used as controls. On days 1, 4, and 7, the medium was replaced with the serum-free medium that contained 10% CCK-8 solution. After a 2 h incubation, the optical density (OD) was measured at 450 nm. Cell viability was calculated using the following equation:

$$Cell\ viability = \frac{OD\ (experiment - blank)}{OD\ (control - blank)} \times 100\,\%$$

2.7. Assessment of hemolysis

For this study, 1 mL of prewashed rabbit blood (2% v/v in BSA) was incubated with 1 mL of 0.2% Triton X-100 (positive control), 1 mL PBS (negative control), and 660 μL PBS containing 340 mg of AHG or APG at 37 °C for 4 h. The vials were then centrifuged at 1000 rpm for 15 min.

The OD values at 545 nm of the resulting supernatant were measured.

2.8. Cell staining and confocal microscopy

Briefly, a hot pre-gel solution made of agarose-PDA was dropped onto the center of the cell culture dish and cooled down under room temperature. After sterilization, cells (MRC-5/RS1) were seeded on the surface of the formed hydrogels (4×10^4 cells).

Cell viability, adhesion, and cellular morphology were evaluated using a Calcein-AM/PI double stain kit. At days 1, 4, and 7, the cells were stained with PI (dead cells, red fluorescence) and Calcein-AM (live cells, green fluorescence) before observation.

Cell spreading was confirmed by imaging filamentous-actin (F-actin), integrin-β1, and cell nuclei. Cell seeded hydrogels were fixed using 4% paraformaldehyde for 10 min at room temperature, washed three times with PBS (10 min), permeabilized with 0.25% Triton X-100/PBS for 10 min, and blocked with 1% BSA for 1 h. For F-actin staining, samples were incubated in the dark with FITC-phalloidin (diluted at 1:200) for 30 min. For integrin-β1 staining, samples were then incubated with rabbit antiβ1-integrin (ab134179, Abcam, diluted at 1:250) overnight at 4 °C. After washing, samples were incubated with goat anti-rabbit integrin secondary antibodies (ab150081, Abcam, diluted at 1:500) for 1 h at room temperature on a shaker. Nuclear DNA was labeled with DAPI. Samples were washed with PBS (three times, 10 min per wash) before observation.

2.9. Evaluation of cell migration in vitro

To assess cell migration by the scratch assay, either MRC-5 or RS1 cells were seeded onto sterilized APG3 hydrogels and 6-well plates (control). Cells were kept at 37 °C until they achieved a 90% confluence. Each well was scratched with a 200 μL pipette tip and washed with PBS to remove the floating cells. Microscopic images were taken immediately after 1, 2, and 3 days scratching. The experiments were repeated three times, and representative images were selected.

To evaluate the cell migration within hydrogels, cells were seeded on the surface of APG3 hydrogel (2×10^5 cells for MRC-5 and 1×10^5 cells for RS1) in 20 mm glass-bottom cell culture dishes. After 24 h of incubation, either RS1 or MRC-5 cells were stained with DiIC18(3) (Solarbio). DiIC18(3) working solution (10 μg/mL) was prepared and added to each dish (500 μL). After 1 h of incubation at 37 °C, cells were washed with culture medium to remove the DiIC18(3)-containing medium. The stained cells were visualized after 1, 2, and 3 days of culture. A series of images was collected through the z-direction from bottom to top, and 3D composite images were created.

2.10. In vitro and in vivo degradation test

In vitro degradation of APG3 was assessed in the following manner: Briefly, 40 mg of APG3 was immersed into PBS. The mixture was kept in a closed centrifuge tube and placed on a shaker (100 rpm) at 37 °C. The hydrogel was taken out and weighed every 10 days. Three parallel experiments were performed to confirm the results.

To evaluate the biodegradability and biocompatibility, APG3 hydrogel slabs (40 mg) were subcutaneously implanted into small pockets on the back of male C57BL/6 mice (8–12 weeks old) for 20 days. The experimental setup included three mice, and each mouse obtained one implant. The body weight of all mice was recorded every three days. After 20 days, the mice were euthanized by CO_2 inhalation and cervical dislocation, and the implants were carefully removed and weighed. The surrounding tissue and vital organs were explanted and immediately fixed in 4% paraformaldehyde (Solarbio, Beijing) for subsequent analysis. Following dehydration and embedding in paraffin, the fixed tissue was cut into 8 μm slice and stained with hematoxylin-eosin (H&E) and Masson's trichrome (MT). The stained samples were imaged by light microscopy (CKX53, Olympus, Japan).

2.11. Wound healing test

The full-thickness skin wound model was used to evaluate the effect of APG3 on wound healing. First, male C57BL/6 mice (8–12 weeks old) were anesthetized and full-thickness round skin defects (8 mm) were created on their back using a hole punch. The wounds were then treated with PBS (control) or APG3 (40 mg), and the mice were individually housed in cages and allowed to heal for two weeks. The wounds were observed on days 0, 3, 7, and 14. On day 14, the mice were sacrificed for histopathological examination (H&E, MT and CD31).

2.12. Statistical analysis

Average ± standard deviation (SD) was used to express the experimental values. One and two-way analysis of variance (ANOVA) was used for statistical analysis. A p-value < 0.05 was considered to be statistically significant (*, for $p < 0.05$; **, for $p < 0.01$ and ***, for $p < 0.001$).

3. Results and discussion

The APG were successfully fabricated through a simple microwave heating-cooling process. The hydrogels were formed with different PDA concentrations (0, 0.05, 0.10, and 0.20 mg/mL), denoted as AHG, APG1, APG2, and APG3, respectively. During the microwave heating-cooling process, the native compact hydrogen bonding between agarose molecules was destroyed. New hydrogen bonding between agarose molecules and water molecules formed, along with the rearrangement of polysaccharide chains, which together led to the construction of a 3D hydrogel network. The APG were formed in less than 10 min (checked by inversion tests).

3.1. Structure and properties of the agarose-PDA hydrogels

3.1.1. Infrared spectroscopy

The FTIR spectra for the pure agarose, PDA, AHG, and APG3 were compared (Fig. 2A). Agarose exhibited absorption bands at 769, 890, and 929 cm^{-1}, attributed to the 3,6-anhydro-β-galactose skeletal bending. The bands of glycosidic linkage and C–O–C of agarose were observed at 1151 and 1040 cm^{-1} [31]. PDA exhibited a characteristic band at 1538 cm^{-1}, which represents the C–N bending vibration of the indolequinone groups [32,33]. Considering the spectra of agarose derived hydrogels (AHG and APG3), it was evident that most adsorption bands were retained as compared with pure agarose. After combination with PDA (APG3), the peak at 1612 cm^{-1} (C–C stretching) became wider, and a new shoulder peak at 1549 cm^{-1} (C–N vibration) appeared.

3.1.2. X-ray diffraction

XRD spectra were recorded to determine the crystalline structure of pure agarose and agarose derived hydrogels (AHG and APG3). According to Figure S2A, an intense peak at $2\theta = 18°$ was observed in the XRD patterns of pure agarose [34]. For AHG and APG3, peak shift was found in their XRD patterns (from 18° to 20°). This was mainly because of the rearrangement of the polysaccharide chains during the gel formation process, leading to a change in the crystalline structure as compared with pure agarose [35]. Also, the characteristic peaks of AHG and APG3 were much weaker compared with agarose, indicating that agarose derived hydrogel exhibited a more amorphous morphology than pure agarose [36].

3.1.3. TGA

The pyrolysis behavior of pure agarose, PDA, AHG, and APG3 was evaluated using TGA (Fig. 2B). An initial loss (10%–15%) of superficial water occurred between 30 and 200 °C for all the samples. For pure agarose, the major weight loss (65%) occurred between 265 and 400 °C,

and this was attributed to the decomposition of the polysaccharide chains. Pure PDA started to lose their weight at about 200 °C and possessed as high as 55.4% mass retention up to 600 °C. The mild pyrolysis process suggested that PDA had the greatest thermal stability among all the tested samples.

The AHG and APG3 exhibited similar pyrolysis behaviors between 230 and 425 °C, indicating the cracking of the polysaccharide chains and PDA chains. Compared with pure agarose, the onset temperature of AHG was postponed from 265 °C to 275 °C and the weight retention rate was decreased from 20.9% to 19.6%. The difference in onset temperature and weight retention rate could be attributed to the rearrangement of agarose chains and newly formed hydrogen bonding inside the hydrogel network. APG3 had the highest content of PDA, resulting in the lowest decomposition temperature (250 °C) and the highest weight retention rate (22.1%) compared with agarose (20.9%) and AHG (19.6%).

3.1.4. Rheological studies

To assess the influence of PDA content on the rheological properties of APG, the corresponding curves of G′ (storage modulus) and G″ (loss modulus) as a function of frequency were recorded (Fig. 2C and Figure S2C). The successful formation of hydrogels was confirmed by G′ > G″ [37–39]. We observed that the value of G′ decreased with the addition of PDA. This can be attributed to the hydrogen bonding interactions between PDA and agarose, which hindered the formation of hydrogen bonds between agarose chains and decreased the hydrogel rigidity [5].

3.1.5. Mechanical studies

Two fundamental mechanical parameters of APG, the compressive strength, and elastic modulus, were assessed using compression tests. The APG exhibited high compressive stress, which resulted from the unique polysaccharide network structures within the agarose (Fig. 2D). The compressive fracture stresses of AHG, APG1, APG2, and APG3 were 0.086, 0.069, 0.060, and 0.057 MPa, respectively. Additionally, the elastic modulus of AHG (0.196 MPa), APG1 (0.175 MPa), APG2 (0.154 MPa), and APG3 (0.148 MPa) were shown in Figure S2C. In our findings, the fracture stress and elastic modulus tended to decrease with an increase in PDA. This result further confirmed that the presence of PDA reduced the strength of APG.

3.1.6. Hydrogel morphology

The FESEM images showed that all of the APG made up of biopolymers had 3D porous structures (Fig. 2E). Interestingly, the pore sizes increased with the rise in PDA content. The average pore size was 33.4, 40.2, 54.7, and 60.1 μm for AHG, APG1, APG2, and APG3, respectively. By comparing these samples, it could be seen that AHG without PDA had the most compact structure. It is expected that the hydrogel with a more compact structure possesses more robust mechanical properties, which is in line with previous results [22,40–42]. The presence of PDA in APG3 was further confirmed by energy-dispersive X-ray (EDX) elemental mapping (Fig. 2E), where single particle analysis revealed the co-presence of carbon, oxygen, and nitrogen elements.

3.1.7. Swelling and de-swelling

The swelling behavior of APG was investigated because the swelling capacity of a hydrogel is related to its biomedical applications [41–44]. Fig. 2F shows the swelling ratio of APG at 25 °C. All the hydrogels absorbed water rapidly at the initial stage (0–50 min) and reached equilibrium after 200 min. The equilibrium swelling value of AHG, APG1, APG2, and APG3 was 30.7, 33.5, 34.5, and 45.1, respectively. Significantly, the swelling capacity was proportional to the PDA content. With increasing PDA content, the pore diameters of the polysaccharide mesh increased, and more space was available for water storage (Fig. 2E). The swelling behavior of APG was further assessed in saline solutions (Fig. 2G and H). All samples revealed a decrease in the swelling degree when soaked in NaCl solutions. However, no significant
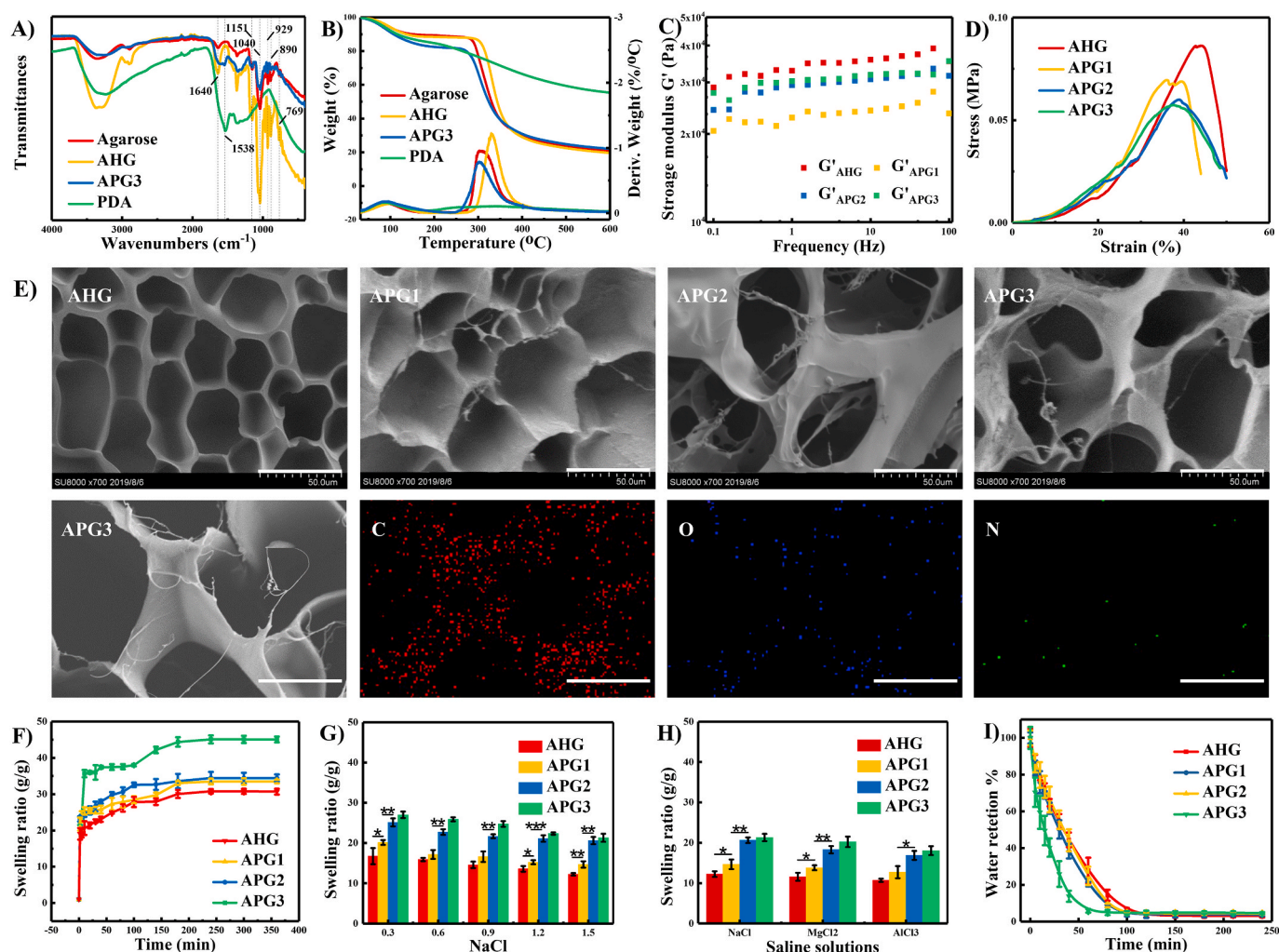
Fig. 2. A) FTIR spectra and B) TGA spectra of agarose, AHG, APG3, and PDA. C) Storage modulus G′ and D) stress and strain curves of APG with different PDA content. E) Representative FESEM images of the lyophilized APG and the EDX mapping images of APG3. Scale bar: 50 μm. The swelling ratio of APG in F) DW, G) NaCl solutions, and H) saline solutions. I) Water retention curves of APG.

difference in the extent of swelling can be observed when increasing the concentration of NaCl or changing the type of salt from NaCl to $MgCl_2$ and $AlCl_3$. This phenomenon can be ascribed to the salt tolerance of agarose, which is the characteristic of neutral polysaccharides [45–47].

The water retention properties of APG are shown in Fig. 2I. Generally, the samples underwent a typical dehydration process and reached a maximum within 100 min. It was evident that the water retention was inversely proportional to the PDA content. At the final state, APG3, with the highest PDA content, had the lowest de-swelling capacity. The relatively loose porous structure might have facilitated the water release [44].

3.2. Biological properties

#### 3.2.1. In vitro biocompatibility evaluation

Excellent biocompatibility of hydrogels is the primary requirement for their use in biological applications [48–50]. To this end, the *in vitro* cytotoxicity of APG was evaluated by the CCK-8 assay using fibroblast cell lines (MRC-5 and RS1, Fig. 3A and B, Figure S3). After 1, 4, and 7 days of incubation with APG, cell viability of more than 70% was retained despite the dosage of dry APG being as high as 3.4 mg/mL. The hemocompatibility of APG was also evaluated, and after incubation of rabbit blood with APG, no hemolysis was observed (Fig. 3D). The quantitative data are presented in Fig. 3C. APG exhibited lower OD values compared with the negative control, indicating excellent

hemocompatibility. These results confirmed that the APG possessed excellent cytocompatibility and blood compatibility, and they could serve as potential candidates for future biological applications such as tissue engineering and regeneration.

3.2.2. Cell adhesion

The APG possessed excellent biocompatibility, and their cell adhesion capabilities increased with the PDA content (Fig. 3F and Figure S4). MRC-5 and RS1 were seeded on the APG. It was observed that cells cultured on the AHG surface maintained a spherical shape (a morphological sign of non-adherence and non-spreading) and weakly adhered to the gel surface throughout this test, indicating that the pure agarose hydrogel did not favor cell adhesion or spreading. However, the rapid spread and proliferation of cells with fibroblastic morphologies was observed with increasing PDA content. On day 4, the cells on PDA-containing hydrogels were elongated and exhibited a more spindle shape, showing structured cytoskeletal networks. The cells covered majority of the total APG3 surface on day 7, and this phenomenon was observed on all three of the other cell types tested (NIH3T3, RS1, and DPSC), and this is shown in Figure S5. It is essential to note that the concentration of PDA determined the adhesion between cells and APG.

To understand how different amounts of PDA impacted cellular attachment to the hydrogel surface, the presence of F-actin and integrin-β1 (transmembrane protein) in MRC-5 and RS1 was determined by fluorescence staining on day 3 of culture (Fig. 3E). As shown in
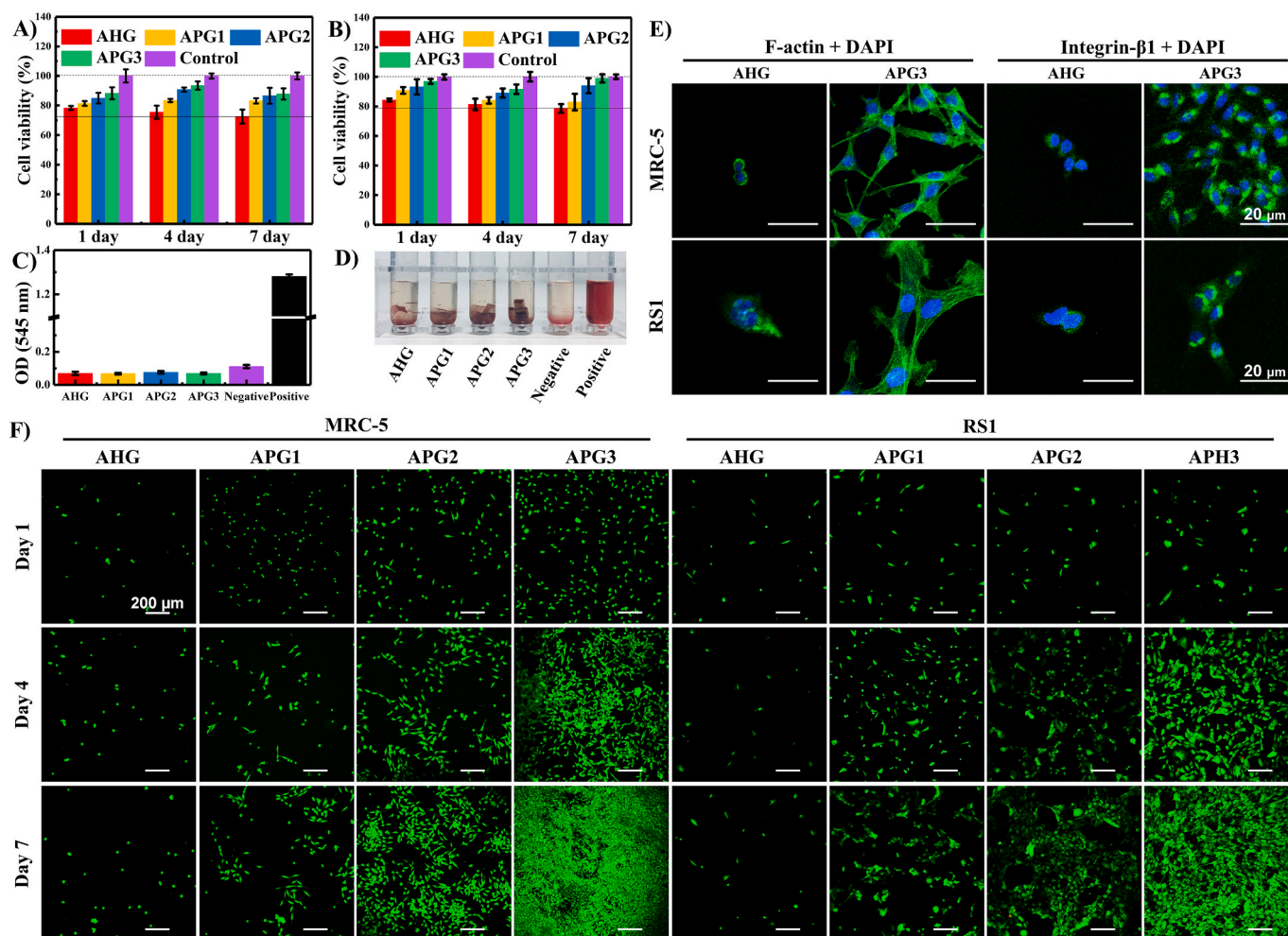
Fig. 3. Cell viability of A) MRC-5 and B) RS1 after 1, 4, and 7 days of incubation with AHG and APG. C–D) Hemolysis evaluation of the APG (340 mg/mL) after incubation with rabbit erythrocytes at 37 °C for 4 h. Negative control: PBS. Positive control: 0.1% Triton X-100. E) Representative images of MRC-5 and RS1 cells on the AHG or APG3 hydrogel surface visualized by FITC-phalloidin/integrin-β1 (green) and DAPI (blue) staining. F) LIVE/DEAD assay showing MRC-5 and RS1 cells adhered to the APG as a function of the PDA content and time.

Fig. 3E, more typical F-actin fibers appeared in the cells adhered to APG3 compared with cells adhered to AHG. It was reported that integrins governed the cell adhesion, and increasing integrin aggregation promoted the formation of F-actin fibers [10,28,51]. As expected, cells cultured on APG3 displayed prominent integrin clustering, while the cells on AHG displayed low levels of integrin clustering (Fig. 3E). These results pointed out the role of PDA in providing a hydrogel matrix for cellular attachment and signaling. The presence of PDA lowered the rigidity of APG, which in turn upregulated the formation of integrin-β1 and F-actin fibers, and facilitated the cell adhesion on the hydrogel.

3.2.3. Cell migration in vitro

To investigate the effect of APG3 scaffolds on cell migration, we conducted an *in vitro* scratch assay. MRC-5/RS1 cells were seeded on APG3 and 6-well plates (control). After scraping, images of the wounds were taken after 0 h, 24 h, 48 h, and 72 h. For control and APG3 groups, both wounds were covered by cells after a 72 h (MRC-5) or 48 h (RS1) culture (Fig. 4A). Cell proliferation and migration at the wound edge co-occurred during wound healing. The cell migration rate of MRC-5 (218 μm/day) and RS1 (327 μm/day) on the surface of APG were greater than that on the surface of cell culture flasks (MRC-5 = 200 μm/day and RS1 = 308 μm/day).

Next, we evaluated the potential of the APG3 hydrogel to serve as a cell delivery vehicle. To do this, we assessed the cell migration of MRC-5 and RS1 inside APG3 (Fig. 4C and Figures S6–S7). As can be seen

from the z-stack images (Fig. 4C), cells migrated inside the hydrogel network after 3 days of incubation. The maximum migration rate of MRC-5 and RS1 through the surface to the inside of APG was 45 μm/day. Together, these results collectively proved that our APG3 hydrogel supported cell adhesion, proliferation, and migration, demonstrating its great potential in tissue engineering.

3.2.4. In vitro/in vivo degradation and biocompatibility of APG3

The *in vitro/in vivo* degradability and biocompatibility of APG3 are critical for its use *in vivo*. The weights of APG3 in PBS were recorded for 40 days (Fig. 5A). As shown in the hydrogel degradation profile, the weight retention ratio of APG3 after 10 days was 98%, after 20 days was 92% after 30 days was 89%, and after 40 days was 84%. These results indicate that the hydrogel progressively degrades at a slow rate. Subcutaneous implantation of the APG3 hydrogel was performed to assess biodegradation and biocompatibility (Fig. 5B and S9). The *in vivo* degradation rate was faster compared with that *in vitro*, and the weight retention ratio of APG3 after 20 days was 84%. The immune responses to the subcutaneously implanted APG3 were determined by H&E and MT stains. Microscope images of the stained surrounding tissue of APG3 are shown in Figure S8. On day 20, full recovery was observed in the surrounding tissue, and inflammatory cells were only found close to the control group. Moreover, tissue morphology on vital organs of lab mice was evaluated through the H&E staining assay (Figure S10). The results showed that all the tissues appeared normal, demonstrating that the
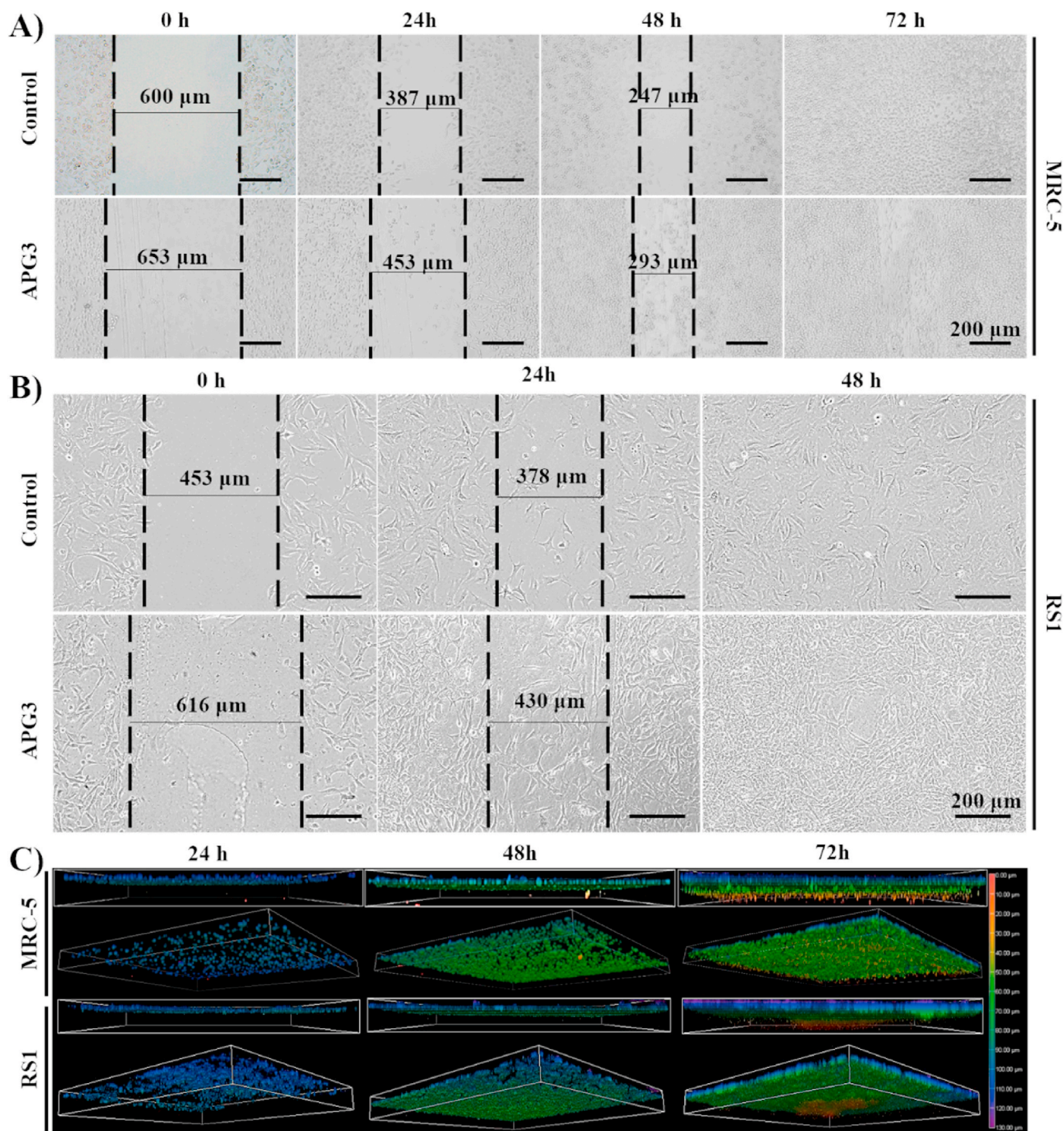
Fig. 4. Cell migration of A) MRC-5 and B) RS1 cells on the surface of APG3 hydrogel and a 6 well plate (set as control). Scale bar: 200 μm. C) Laser scanning confocal microscope (LSCM) 3D stacking images of cell-laden APG3 hydrogels with a thickness of 130 μm, showing the distribution of MRC-5 and RS1 cells after 1, 2, and 3 days of cell culture.

APG3 hydrogel had no systemic toxic effect on the host vital organs.

3.2.5. Wound healing in vivo

The above results demonstrated that the APG3 had excellent bio-compatibility, cell adhesion, and biodegradability, which were beneficial for the skin tissue engineering. To further prove the potency of APG3 in this aspect, APG3 (PBS as control) was applied to full-thickness skin defect models (8 mm). Fig. 5D shows the macroscopic view of the wounds on day 3, day 7 and day 14. The wound closure rate was higher in the APG3-treated mouse than in the control group. Histological analysis was performed 14 days after wound dressing to observe the initial re-epithelialization and collagen production (Fig. 5F). Hema-toxylin and eosin (H&E) staining confirmed that the APG3-treated group induced thicker skin regeneration (1177 μm) compared with the control group (960 μm). Masson's trichrome (MT) staining revealed that the collagen density in the wound bed was increased in the APG3-treated mice (Fig. 5F–5G) and the increased collagen deposition was essential for tissue remodeling and fibrosis. The angiogenic responses of
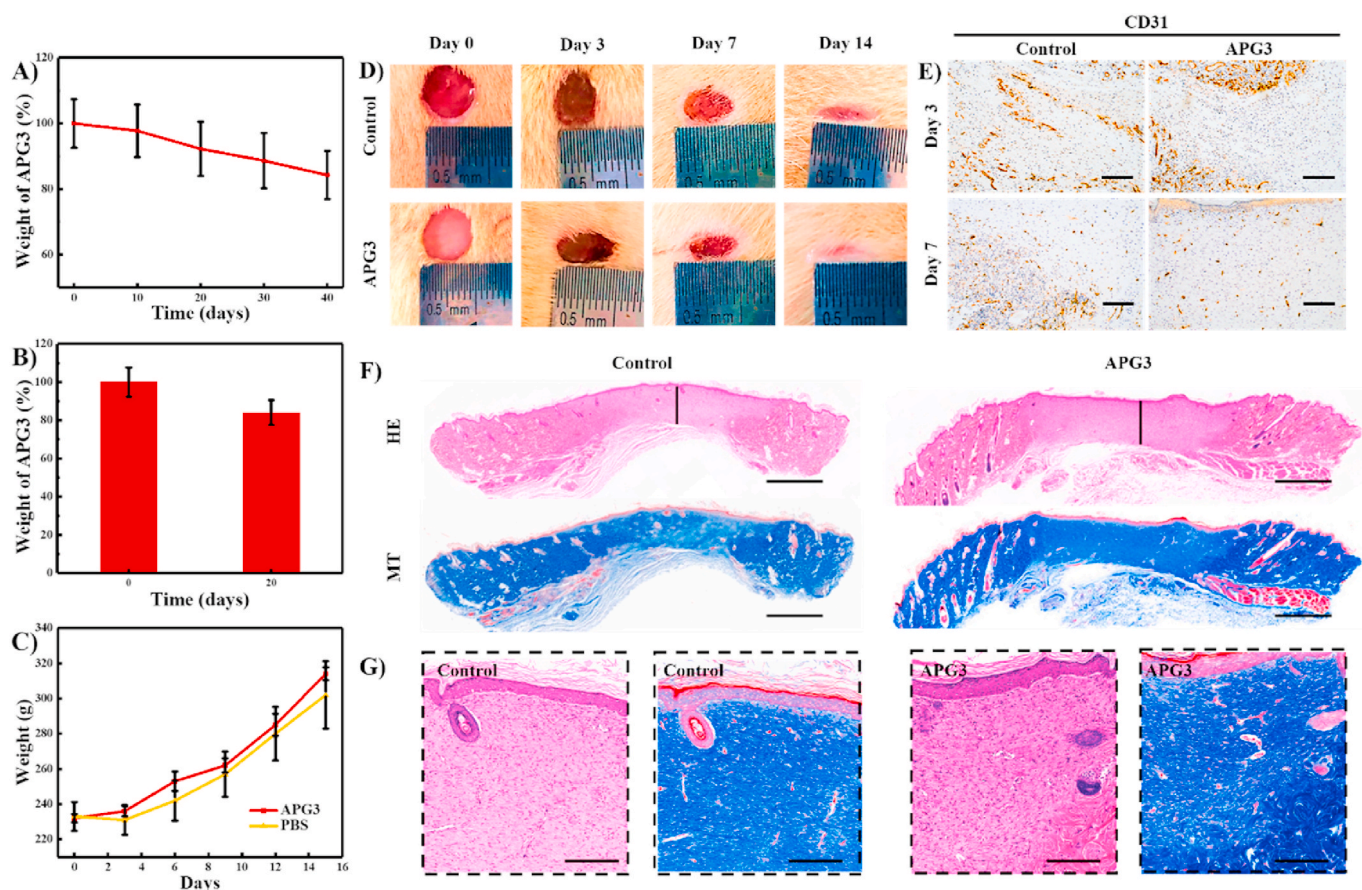
Fig. 5. A) Degradation profiles of APG3 in PBS at 37 °C for 40 days. B) Degradation profiles of APG3 *in vivo* for 20 days. C) Body weight of lab mice for 20 days after the implantation. Weight loss was hardly observed in all mice for 20 days after the implantation. D) Representative photos of the skin wounds treated with PBS (control) and APG3. E) CD31 immunostaining of wounds after 3 and 7 days. Scale bars: 200 μm. F) Representative H&E staining and MT staining of wounds after 14 days. Scale bars: 2000 μm. G) High magnification imaging of wound beds. Scale bars: 200 μm.

APG3 were determined by CD31 staining in the regenerated tissues on day 3 and day 7 (Fig. 5E). Compared to the control group, APG3 group showed higher CD31 expression on the day 3. With the prolongation of wound healing time, at day 7, both groups showed decreased CD31 expression, and APG3 group still presented higher CD31 expression. We assumed that the APG3 hydrogel could maintain moist healing environment, which prevented tissue dehydration and cell death. Besides, APG3 with good cell affinity might offer a good platform to facilitate cell adhesion, migration and growth, which in turn promoted collagen deposition and angiogenesis, thereby accelerating wound repair [52–55]. These results demonstrated that APG3 was an ideal scaffold for skin tissue engineering.

4. Conclusions

In summary, we have presented a flexible strategy to generate a functional APG scaffold with good cell adhesion, biodegradability and biocompatibility. Through the introduction of PDA, the rigidity of APG was decreased and APG was endowed with excellent cell adhesion capability. *In vitro* experiments proved that cell migration rate on the surface of APG3 was high, and cells could penetrate into the network of APG3. Notably, the wound healing process of full-thickness skin defect could be accelerated by using APG3 to promote collagen deposition and vascularization. The strategy outlined here is not only limited to repair skin wound, but also has great potential for application in other areas of tissue engineering.

CRediT authorship contribution statement

Ting Su: Conceptualization, Data curation, Formal analysis, Visualization, Writing - original draft. **Mengying Zhang:** Investigation. **Qiankun Zeng:** Methodology. **Wenhao Pan:** Software. **Yijing Huang:** Investigation. **Yuna Qian:** Validation. **Wei Dong:** Supervision. **Xiaoliang Qi:** Project administration, Writing - review & editing. **Jianliang Shen:** Funding acquisition, Project administration.

Declaration of competing interest

The authors declare no conflict of interest.

Acknowledgements

Appendix A. Supplementary data

Supplementary data to this article can be found online at https://doi.org/10.1016/j.bioactmat.2020.09.004.

References

[1] L. Zhang, X. Zuo, S. Lia, M. Sun, H. Xie, K. Zhang, J. Zhou, L. Che, J. Ma, Z. Jia, Synergistic therapy of magnetism-responsive hydrogel for soft tissue injuries, Bioact. Mater. 4 (2019) 160–166.

[2] A. Pal, B.L. Vernon, M. Nikkhah, Therapeutic neovascularization promoted by injectable hydrogels, Bioact. Mater. 3 (2018) 389–400.

[3] T.E.L. Douglas, M. Dziadek, S. Gorodzha, J. Liskova, G. Brackman, V. Vanhoorne, C. Vervaet, L. Balcaen, M.D.R.F. Garcia, A.R. Boccaccini, V. Weinhardt, T. Baumbach, F. Vanhaecke, T. Coenye, L. Bacakova, M.A. Surmeneva, R.A. Surmenev, K. Cholewa-Kowalska, A.G. Skirtach, Novel injectable gellan gum hydrogel composites incorporating Zn- and Sr-enriched bioactive glass microparticles: high-resolution X-ray microcomputed tomography, antibacterial and in vitro testing, J. Tissue Eng. Regen. Med. 12 (2018) 1313–1326.

[4] G. Zhong, J. Yao, X. Huang, Y. Luo, M. Wang, J. Han, F. Chen, Y. Yu, Injectable ECM hydrogel for delivery of BMSCs enabled full-thickness meniscus repair in an orthotopic rat model, Bioact. Mater. 5 (2020) 871–879.

[5] G.C. Ingavle, S.H. Gehrke, M.S. Detamore, The bioactivity of agarose-PEGDA interpenetrating network hydrogels with covalently immobilized RGD peptides and physically entrapped aggrecan, Biomaterials 35 (2014) 3558–3570.

[6] O. Chaudhuri, J.C. White, P.A. Janmey, D.J. Mooney, V.B. Shenoy, Effects of extracellular matrix viscoelasticity on cellular behaviour, Nature 584 (2020) 535–546.

[7] B. Yang, H. Wolfenson, V.Y. Chung, N. Nakazawa, S. Liu, J. Hu, R.Y.J. Huang, M.P. Sheetz, Stopping transformed cancer cell growth by rigidity sensing, Nat. Mater. 19 (2019) 239–250.

[8] M. Chen, J. Zhang, P. Zhou, X. Liu, H. Zhao, X. Zhou, Q. Gu, B. Li, X. Zhu, Q. Shi, Substrate stiffness modulates bone marrow-derived macrophage polarization through NF-κB signaling pathway, Bioact. Mater. 5 (2020) 880–890.

[9] W. Huang, Y. Wang, Z. Huang, X. Wang, L. Chen, Y. Zhang, L. Zhang, On-demand dissolvable self-healing hydrogel based on carboxymethyl chitosan and cellulose nanocrystal for deep partial thickness burn wound healing, ACS Appl. Mater. Interfaces 10 (2018) 41076–41088.

[10] X. Qi, T. Su, M. Zhang, X. Tong, W. Pan, Q. Zeng, Z. Zhou, L. Shen, X. He, J. Shen, Macroporous hydrogel scaffolds with tunable physicochemical properties for tissue engineering constructed using renewable polysaccharides, ACS Appl. Mater. Interfaces 12 (2020) 13256–13264.

[11] S. Huang, C. Wang, J. Xu, L. Ma, C. Gao, In situ assembly of fibrinogen/hyaluronic acid hydrogel via knob-hole interaction for 3D cellular engineering, Bioact. Mater. 2 (2017) 253–259.

[12] Z. Shen, S. Kuang, Y. Zhang, M. Yang, W. Qin, X. Shi, Z. Lina, Chitosan hydrogel incorporated with dental pulp stem cell-derived exosomes alleviates periodontitis in mice via a macrophage-dependent mechanism, Bioact. Mater. 5 (2020) 1113–1126.

[13] L. Cheng, Z. Cai, J. Zhao, F. Wang, M. Lu, L. Deng, W. Cui, Black phosphorus-based 2D materials for bone therapy, Bioact. Mater. 5 (2020) 1026–1043.

[14] W. Yuan, Z. Li, X. Xie, Z.Y. Zhang, L. Bian, Bisphosphonate-based nanocomposite hydrogels for biomedical applications, Bioact. Mater. 5 (2020) 819–831.

[15] J. Chi, X. Zhang, C. Chen, C. Shao, Y. Zhao, Y. Wang, Antibacterial and angiogenic chitosan microneedle array patch for promoting wound healing, Bioact. Mater. 5 (2020) 253–259.

[16] X. Jiang, S. Wu, M. Kuss, Y. Kong, W. Shi, P.N. Streubel, T. Li, B. Duan, 3D printing of multilayered scaffolds for rotator cuff tendon regeneration, Bioact. Mater. 5 (2020) 636–643.

[17] T. Figueiredo, J. Jing, I. Jeacomine, J. Olsson, T. Gerfaud, J.G. Boiteau, C. Rome, C. Harris, R. Auzely-Velty, Injectable self-healing hydrogels based on boronate ester formation between hyaluronic acid partners modified with benzoxaborin derivatives and saccharides, Biomacromolecules 21 (2019) 230–239.

[18] Y. Tang, X. Cai, Y. Xiang, Y. Zhao, X. Zhang, Z. Wu, Cross-linked antifouling polysaccharide hydrogel coating as extracellular matrix mimics for wound healing, J. Mater. Chem. B 5 (2017) 2989–2999.

[19] J.D. Schneible, A. Singhal, R.L. Lilova, C.K. Hall, A. Grafmuller, S. Menegatti, Tailoring the chemical modification of chitosan hydrogels to fine-tune the release of a synergistic combination of chemotherapeutics, Biomacromolecules 20 (2019) 3126–3141.

[20] Y. Chen, L. Yu, B. Zhang, W. Feng, M. Xu, L. Gao, N. Liu, Q. Wang, X. Huang, P. Li, W. Huang, Design and synthesis of biocompatible, hemocompatible, and highly selective antimicrobial cationic peptidopolysaccharides via click Chemistry, Biomacromolecules 20 (2019) 2230–2240.

[21] J. Xu, G. Wang, Y. Wu, X. Ren, G. Gao, Ultrastretchable wearable strain and pressure sensors based on adhesive, tough, and self-healing hydrogels for human motion monitoring, ACS Appl. Mater. Interfaces 11 (2019) 25613–25623.

[22] P. Tang, L. Han, P. Li, Z. Jia, K. Wang, H. Zhang, H. Tan, T. Guo, X. Lu, Mussel-inspired electroactive and antioxidative scaffolds with incorporation of polydopamine-reduced graphene oxide for enhancing skin wound healing, ACS Appl. Mater. Interfaces 11 (2019) 7703–7714.

[23] X. Qi, Q. Zeng, X. Tong, T. Su, L. Xie, K. Yuan, J. Xu, J. Shen, Polydopamine/montmorillonite-embedded pullulan hydrogels as efficient adsorbents for removing crystal violet, J. Hazard Mater. 402 (2021) 123359.

[24] Y. Liang, X. Zhao, T. Hu, B. Chen, Z. Yin, P.X. Ma, B. Guo, Adhesive hemostatic conducting injectable composite hydrogels with sustained drug release and photothermal antibacterial activity to promote full-thickness skin regeneration during wound healing, Small 15 (2019) 1900046.

[25] M.M. Hasani-Sadrabadi, P. Sarrion, N. Nakatsuka, T.D. Young, N. Taghdiri, S. Ansari, T. Aghaloo, S. Li, A. Khademhosseini, P.S. Weiss, A. Moshaverinia, Hierarchically patterned polydopamine-containing membranes for periodontal tissue engineering, ACS Nano 13 (2019) 3830–3838.

[26] W. Cheng, X. Zeng, H. Chen, Z. Li, W. Zeng, L. Mei, Y. Zhao, Versatile polydopamine platforms: synthesis and promising applications for surface modification and advanced nanomedicine, ACS Nano (2019) 8537–8565.

[27] S. Pacelli, K. Rampetsreiter, S. Modaresi, S. Subham, A.R. Chakravarti, S. Lohfeld, M.S. Detamore, A. Paul, Fabrication of a double-cross-linked interpenetrating polymeric network (IPN) hydrogel surface modified with polydopamine to modulate the osteogenic differentiation of adipose-derived stem cells, ACS Appl. Mater. Interfaces 10 (2018) 24955–24962.

[28] Z. Tang, F. Jiang, Y. Zhang, Y. Zhang, YuanYang, X. Huang, Y. Wang, D. Zhang, N. Ni, F. Liu, M. Luo, X. Fan, W. Zhang, P. Gu, Mussel-inspired injectable hydrogel and its counterpart for actuating proliferation and neuronal differentiation of retinal progenitor cells, Biomaterials 194 (2019) 57–72.

[29] Y. Luo, X. Lin, B. Chen, X. Wei, Cell-laden 4D bioprinting using NIR-triggered shape morphing alginate/polydopamine bioinks, Biofabrication 11 (2019) 045019.

[30] A. Jin, Y. Wang, K. Lin, L. Jiang, Nanoparticles modified by polydopamine: working as "drug" carriers, Bioact. Mater 5 (2020) 522–541.

[31] X. Qi, T. Su, X. Tong, W. Xiong, Q. Zeng, Y. Qian, Z. Zhou, X. Wu, Z. Li, L. She, X. He, C. Xu, M. Chen, Y. Li, J. Shen, Facile formation of salecan/agarose hydrogels with tunable structural properties for cell culture, Carbohydr. Polym. 224 (2019) 115208.

[32] J. Zhao, L. Bai, X.K. Ren, J. Guo, S. Xia, W. Zhang, Y. Feng, Co-immobilization of ACH11 antithrombotic peptide and CAG cell-adhesive peptide onto vascular grafts for improved hemocompatibility and endothelialization, Acta Biomater. 97 (2019) 344–359.

[33] R.M. Felfel, M.J. Gideon-Adeniyi, K.M.H. Zakir, G.A.F. Roberts, D.M. Grant, Structural, mechanical and swelling characteristics of 3D scaffolds from chitosan-agarose blends, Carbohydr. Polym. 204 (2019) 59–67.

[34] A. GhavamiNejad, C.H. Park, C.S. Kim, In situ synthesis of antimicrobial silver nanoparticles within antifouling zwitterionic hydrogels by catecholic redox Chemistry for wound healing application, Biomacromolecules 17 (2016) 1213–1223.

[35] N. Li, C. Liu, W. Chen, Facile access to guar gum based supramolecular hydrogels with rapid self-healing ability and multistimuli responsive gel-sol transitions, J. Agric. Food Chem. 67 (2019) 746–752.

[36] J. Song, H. Zhao, G. Zhao, Y. Xiang, Y. Liu, Novel semi-IPN nanocomposites with functions of both nutrient slow-release and water retention. 1. Microscopic structure, water absorbency, and degradation performance, J. Agric. Food Chem. 67 (2019) 7587–7597.

[37] C. Zhao, N.T. Qazvini, M. Sadati, Z. Zeng, S. Huang, A.L. De La Lastra, L. Zhang, Y. Feng, W. Liu, B. Huang, B. Zhang, Z. Dai, Y. Shen, X. Wang, W. Luo, B. Liu, Y. Lei, Z. Ye, L. Zhao, D. Cao, L. Yang, X. Chen, A. Athiviraham, M.J. Lee, J.M. Wolf, R.R. Reid, M. Tirrell, W. Huang, J.J. de Pablo, T.C. He, A pH-triggered, self-assembled, and bioprintable hybrid hydrogel scaffold for mesenchymal stem cell based bone tissue engineering, ACS Appl. Mater. Interfaces 11 (2019) 8749–8762.

[38] S. Zhang, Y. Zhang, B. Li, P. Zhang, L. Kan, G. Wang, H. Wei, X. Zhang, N. Ma, One-step preparation of highly stretchable, conductive and transparent polyvinyl alcohol-phytic acid hydrogel for casual writing circuits, ACS Appl. Mater. Interfaces 11 (2019) 32441–32448.

[39] J. Zeng, D. Shi, Y. Gu, T. Kaneko, L. Zhang, H. Zhang, D. Kaneko, M. Chen, Injectable and NIR-responsive hydrogels encapsulating dopamine-stabilized gold nanorods with long photothermal activity controlled for tumor therapy, Biomacromolecules 20 (2019) 17256–17269.

[40] H. Maleki, M.A. Shahbazi, S. Montes, S.H. Hosseini, M.R. Eskandari, S. Zaunschirm, T. Verwanger, S. Mathur, B. Milow, B. Krammer, N. Husing, Mechanically strong silica-silk fibroin bioaerogel: a hybrid scaffold with ordered honeycomb micromorphology and multiscale porosity for bone regeneration, ACS Appl. Mater. Interfaces 11 (2019) 17256–17269.

[41] X. Liu, Q. Zhang, L. Duan, G. Gao, Bioinspired nucleobase-driven nonswellable adhesive and tough gel with excellent underwater adhesion, ACS Appl. Mater. Interfaces 11 (2019) 6644–6651.

[42] M. Zhang, S. Chen, N. Sheng, B. Wang, J. Yao, Z. Wu, H. Wang, A strategy of tailoring polymorphs and nanostructures to construct self-reinforced nonswelling high-strength bacterial cellulose hydrogels, Nanoscale 11 (2019) 15347–15358.

[43] C.S. Chen, F. Zeng, X. Xiao, Z. Wang, X.L. Li, R.W. Tan, W.Q. Liu, Y.S. Zhang, Z.D. She, S.J. Li, Three-dimensionally printed silk-sericin-based hydrogel scaffold: a promising visualized dressing material for real-time monitoring of wounds, ACS Appl. Mater. Interfaces 10 (2018) 33879–33890.

[44] X. Qi, Y. Yuan, J. Zhang, J.W.M. Bulte, W. Dong, Oral administration of salecan-based hydrogels for controlled insulin delivery, J. Agric. Food Chem. 66 (2018) 10479–10489.

[45] F. Yu, T. Cui, C. Yang, X. Dai, J. Ma, κ-Carrageenan/Sodium alginate double-network hydrogel with enhanced mechanical properties, anti-swelling, and adsorption capacity, Chemosphere 237 (2019) 124417.

[46] T. Su, L. Wu, X. Pan, C. Zhang, M. Shi, R. Gao, X. Qi, W. Dong, Pullulan-derived nanocomposite hydrogels for wastewater remediation: synthesis and characterization, J. Colloid Interface Sci. 542 (2019) 253–262.

[47] T. Su, X. Qi, G. Zuo, X. Pan, J. Zhang, Z. Han, W. Dong, Polysaccharide metallo-hydrogel obtained from Salecan and trivalent chromium: synthesis and characterization, Carbohydr. Polym. 181 (2018) 285–291.

[48] Z. Bao, C. Xian, Q. Yuan, G. Liu, J. Wu, Natural polymer-based hydrogels with enhanced mechanical performances: preparation, structure, and property, Adv. Healthc. Mater (2019) 1900670.

[49] H. Liu, J. Liu, C. Qi, Y. Fang, L. Zhang, R. Zhuo, X. Jiang, Thermosensitive injectable in-situ forming carboxymethyl chitin hydrogel for three-dimensional cell culture, Acta Biomater. 35 (2016) 228–237.

[50] K.D. Waduthanthri, Y. He, C. Montemagno, S. Cetinel, An injectable peptide hydrogel for reconstruction of the human trabecular meshwork, Acta Biomater. 100 (2019) 244–254.

[51] A.E. Stanton, X. Tong, S. Lee, F. Yang, Biochemical ligand density regulates yes-associated protein translocation in stem cells through cytoskeletal tension and integrins, ACS Appl. Mater. Interfaces 11 (2019) 8849–8857.

[52] L. Schirmer, K. Chwalek, M.V. Tsurkan, U. Freudenberg, C. Werner, Glycosaminoglycan-based hydrogels with programmable host reactions, Biomaterials 228 (2020) 119557.

[53] G. Chen, Y. Yu, X. Wu, G. Wang, J. Ren, Y. Zhao, Bioinspired multifunctional hybrid hydrogel promotes wound healing, Adv. Funct. Mater. 28 (2018) 1801386.

[54] X. Zhao, Y. Liang, Y. Huang, J. He, Y. Han, B. Guo, Physical double-network hydrogel adhesives with rapid shape adaptability, fast self-healing, antioxidant and NIR/pH stimulus-responsiveness for multidrug-resistant bacterial infection and removable wound dressing, Adv. Funct. Mater. 30 (2020) 1910748.

[55] J.M. Grolman, M. Singh, D.J. Mooney, E. Eriksson, K. Nuutila, Antibiotic-containing agarose hydrogel for wound and burn care, J. Burn Care Res. 40 (2019) 900–906.